https://doi.org/10.5194/egusphere-2026-4701
Preprint. Discussion started: 14 August 2026


# Beyond Spectral Smile: Comprehensive Imaging Spectrometer Wavelength Calibration from Atmospheric Features

Mads J. Ahlebæk[1,2], David R. Thompson[2], Regina F. Eckert[2], Philip Brodrick[2], Mads T. Frandsen[1], and Robert O. Green[2]

[1]University of Southern Denmark - Campusvej 55, 5230 Odense, Danmark
[2]Jet Propulsion Laboratory, California Institute of Technology - 4800 Oak Grove Dr, Pasadena, CA 91109, USA

**Correspondence:** Mads J. Ahlebæk (ahle@sdu.dk)

**Abstract.** Accurate spectral calibration is essential for quantitative imaging spectroscopy, as even sub-nanometer wavelength errors can propagate into atmospheric correction and surface-property retrievals. Existing approaches for in-flight wavelength calibration typically assume simplified spectral parameterizations, limiting the complexity of wavelength variations that can be recovered from atmospheric absorption features. In this study, we investigate the information content of visible-to-shortwave infrared (VSWIR) observations for constraining instrument wavelength calibration using a Bayesian maximum a posteriori retrieval framework. Using nine high signal-to-noise EMIT (Earth Surface Mineral Dust Source Investigation) scenes acquired over spectrally homogeneous desert targets, we systematically evaluate spline-based wavelength calibration models with varying numbers and placements of spline knot points. Model performance is assessed using agreement with Zemax optical simulations, solution consistency across independent scenes, and leave-one-out cross-validation. All three evaluation criteria identify a four-knot spline representation as the optimal balance between model flexibility and stability, whereas more complex parameterizations exhibit increased sensitivity to knot placement and reduced reproducibility. Applying this optimal configuration independently across the detector array reveals coherent cross-track wavelength-dispersion variations that cannot be adequately represented by traditional uniform or simple spectral-smile corrections. Although the retrieved spatial variations are small—typically on the order of 1% of a spectral channel width—they exhibit a structured saddle-shaped pattern that is consistent across scenes and indicative of genuine instrument behavior. These results demonstrate that atmospheric absorption features provide sufficient information to retrieve spatially varying wavelength calibration for modern VSWIR imaging spectrometers, supporting more accurate radiometric processing and motivating spatially resolved spectral calibration strategies for current and future spaceborne missions.

## 1 Introduction

Remote imaging spectroscopy in the visible to shortwave infrared (VSWIR) is sensitive to diverse atmospheric and surface phenomena, enabling a single instrument to address numerous agricultural, geologic, and water use applications (Haboudane et al., 2002; van der Meer et al., 2012; Yang et al., 2022; Thompson et al., 2026). By splitting solar-reflected light into hundreds of contiguous spectral channels, spectrometers can identify and quantify unique compounds on the Earth's surface. They allow

https://doi.org/10.5194/egusphere-2026-4701
Preprint. Discussion started: 14 August 2026


analysts to fit physics-based models of the scene that explain the observed measurement as a physical combination of absorbing and scattering materials. The ability stands apart from traditional multiband instruments, which generally rely on empirical or correlational relationships between band combinations and the phenomena of interest.

Accurate spectroscopy relies on a foundation of accurate spectral and radiometric calibration. Enormous progress has been made in recent years in building instruments that remain optomechanically stable, dramatically simplifying the calibration challenge. Similarly, progress has been made in in-flight calibration, enabling radiometric and spectral parameters to be tracked with high accuracy using features of the surface and atmosphere. However, as instruments become ever more precise and investigators pursue ever subtler phenomena at the edge of instrument noise, we must continuously improve our calibration processes to keep pace, so that calibration does not become a bottleneck to scientific and applied outcomes. With the number of sensors increasing, robust automated approaches to track instrument calibration across thermal cycles are increasingly important.

One area with potential for improvement is instrument spectral calibration. Sensor spectral calibration can drift with thermal cycles and gravity unloading, as the optical components move by microns relative to their original laboratory positions. Traditionally, the spectral response function of each channel has been divided into two aspects: first, the center wavelength of the response; and second, the distribution of sensitivity about that center wavelength. Since both can shift over time, it is important to regularly track and update these parameters throughout the sensor's lifespan. Researchers have used atmospheric features as an opportunistic wavelength standard, fitting gas absorptions with radiative transfer models to recover both parameters from flight data (Gao et al., 2004; Guanter et al., 2006; D'Odorico et al., 2010; Kuhlmann et al., 2016; Thompson et al., 2018a). Most often, analysts have applied these models over a restricted range of parameters - for example, by assuming that calibration is uniform in the across-track dimension, or that the change in wavelength position can be represented by a low-order polynomial in channel number. These restrictions compensate for the finite number of discrete atmospheric absorption features available to drive the fitting process.

Here, we take this approach to its logical extreme by independently identifying the wavelength-center channel for each element in the focal plane array. We aim to determine the limits of wavelength calibration with VSWIR atmospheric features - in other words, how accurate atmospheric calibration can be with wavelength dispersions that are more complex and nonuniform. This will inform future efforts for vicarious imaging spectrometer calibration from atmospheric features. We apply this approach to a representative dataset from NASA's Earth Surface Mineral Dust Source Investigation (EMIT), which is onboard the International Space Station. Our analysis indicates that the Visible-Shortwave Infrared (VSWIR) range contains rich information for constraining wavelength calibrations that are not constant in cross-track or spectral dimensions. We find that, while there is a natural limit to the complexity of spectral and spatial nonuniformities that the data can reliably estimate, the VSWIR range is more than sufficient to constrain the wavelength calibration of modern imaging spectrometers with EMIT-like spectral sampling.

https://doi.org/10.5194/egusphere-2026-4701
Preprint. Discussion started: 14 August 2026


## 2 Instrument and Dataset

### 2.1 EMIT - Earth surface Mineral dust source InvesTigation

EMIT is a spaceborne imaging spectrometer deployed on the International Space Station (ISS) to measure the spectral reflectance of Earth's land surface in the visible to shortwave infrared (VSWIR) wavelength range ($380\,\mathrm{nm}$–$2500\,\mathrm{nm}$). EMIT employs a pushbroom spectrometer design that acquires contiguous spectra across a wide swath, enabling high-fidelity surface mapping at regional to global scales. The optical design is described in Bradley et al. (2020), while the calibration and on-orbit performance are presented in Thompson et al. (2024). In brief and approximate numbers, EMIT provides measurements at a spatial resolution of $62\,\mathrm{m}$ at a $400\,\mathrm{km}$ orbital altitude, with $7.4\,\mathrm{nm}$ spectral sampling across $285$ spectral channels. The instrument features a cryo-cooled focal plane array sensor with $1280 \times 480$ pixels of $30\,\mu\mathrm{m}$ pitch, yielding a swath width of approximately $80\,\mathrm{km}$ (corresponding to an $11^{\circ}$ field of view). These characteristics enable EMIT to resolve diagnostic absorption features of surface materials while maintaining sufficient spatial coverage for global analyses. EMIT was originally selected to map the surface mineralogy of arid lands and characterize mineral dust composition. However, following the completion of this primary mission, it has begun mapping the entire terrestrial landmass accessible to the ISS. It has been used for a wide range of applications, ranging from water resources Scrivner et al. (2025), to the cryosphere Bohn et al. (2025), to atmospheric science Thorpe et al. (2023).

### 2.2 Dataset Description

The analysis presented in this study is based on a selected set of nine EMIT datacubes acquired over arid and semi-arid regions characterized by spectrally uniform, spatially extensive, and relatively flat surfaces. These sites were chosen to provide high signal-to-noise ratio (SNR) measurements. Their bright, homogeneous surfaces maximize the signal recorded by the sensor, while minimizing the influence of sub-pixel variability and surface heterogeneity on the observed spectra. The selected scenes span Northern Africa (Algeria, Tunisia, Sudan, Niger, Libya) and Saudi Arabia, and are captured primarily in late 2025, with the exception of *Scene 6* acquired in March 2025. All images are publicly available through NASA's Earthdata platform and can be accessed via the Earthdata Search portal (https://search.earthdata.nasa.gov/search). All images are L1B radiance products, non-orthorectified, and were averaged along the down-track dimension to further improve SNR while preserving the effects of cross-track variability. RGB representations of the scenes are shown in Fig. 1, and their corresponding longitude, latitude, and Granule IDs are summarized in Table 1. For completeness, the Granule ID for *Scene 1* (EMIT20250815T124114) encodes the acquisition date and time: the first eight digits (20250815) indicate 15 August 2025, and the final six digits (124114) give the UTC acquisition time 12:41:14.

Since EMIT calibration could hypothetically drift over time, we designed the experiment to focus on a narrow time range. This allowed us to assess consistency between different calibration attempts on an effectively identical instrument. Telemetry over this time range indicated standard thermal control, with spectrometer and detector array temperatures held to a tight operating range. Although each scene was from a different geographic region, they consisted almost entirely of bare soil, which minimized the influence of surface changes, such as vegetation growth or moisture variability, on the independent calibration

https://doi.org/10.5194/egusphere-2026-4701
Preprint. Discussion started: 14 August 2026


| Scene | Granule ID | Lat (° N) | Lon (° E) |
|---|---|---|---|
| Scene 1 | emit20250815T124114 | 32.16 | 8.79 |
| Scene 2 | emit20251022T100513 | 29.63 | 7.55 |
| Scene 3 | emit20251215T124622 | 32.43 | 2.61 |
| Scene 4 | emit20250826T084042 | 24.62 | 13.08 |
| Scene 5 | emit20251130T100813 | 30.71 | 9.84 |
| Scene 6 | emit20250324T124919 | 24.41 | 12.61 |
| Scene 7 | emit20251025T092041 | 20.69 | 10.34 |
| Scene 8 | emit20251127T091851 | 21.12 | 29.82 |
| Scene 9 | emit20251127T074538 | 20.20 | 52.64 |

**Table 1.** Geographic locations and Granule IDs of EMIT scenes used in this study. Coordinates correspond to the approximate scene center.

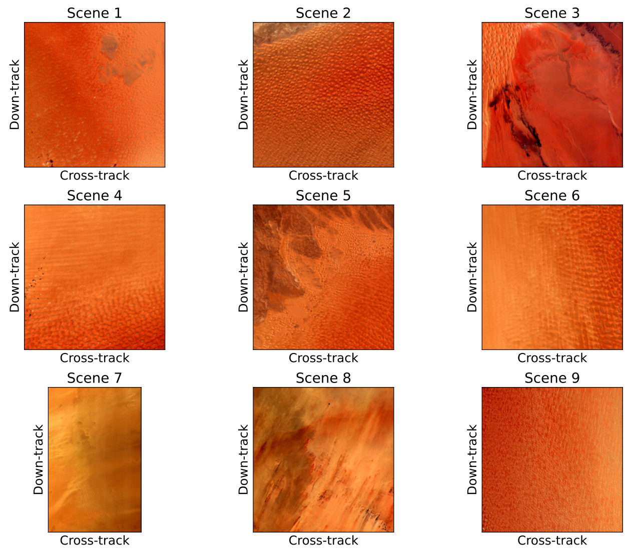


**Figure 1.** RGB views of the nine EMIT datacubes selected for analysis in this study.

attempts. The combination of high SNR, spatial uniformity, and controlled temporal variability enables a robust evaluation of the dataset for the objectives of this study.

#### 2.2.1 Data Preparation

The acquired images were preprocessed by averaging in the down-track direction and bin-averaging in the cross-track direction. As a result, the data provided to our analysis (Section 3.1) no longer represent conventional image cubes, but instead have dimensions of $(1 \times 69 \times 285)$ in the down-track, cross-track, and spectral directions, respectively.

This preprocessing approach aggregates spatial information along the down-track dimension, thereby emphasizing instrument-specific spectral responses and reducing random noise. Consequently, the signal-to-noise ratio improves, enhancing the stability and reliability of the wavelength calibration retrievals.

The sensor has a total cross-track width of 1242 pixels, enabling uniform bin averaging with a bin size of 18 pixels. This operation reduces the effective spatial dimensionality from 1242 to 69 pixels while reducing the measurement noise at each location. Because the wavelength offset is a smooth function of cross-track position, this preprocessing step should not affect the calibration result.

## 3 Methodology

### 3.1 Retrieval Framework

We estimate instrument parameters with a Bayesian Maximum A Posteriori (MAP) model inversion approach. We use the ISOFIT (Imaging Spectrometer Optimal FITting) codebase, a physics-based, open-source Python library (Brodrick et al., 2026) for estimating surface and atmospheric properties from spectral imagery. The codebase builds on work by Thompson et al. (2018b), and includes radiative transfer emulation by Brodrick et al. (2021). The approach plays a central role in many NASA missions, including AVIRIS, EMIT, and an upcoming global VSWIR imaging spectroscopy mission. A key strength of probabilistic model inversion is that, rather than simply removing atmospheric contributions from measured spectra, it jointly estimates surface and atmospheric parameters within a unified and physically consistent retrieval framework.

Mathematically, the approach draws from the Optimal Estimation (OE) framework pioneered by Rodgers (2000). At its core is a forward model $F(\mathbf{x})$, which maps a set of unknown physical parameters, defined in the state vector $\mathbf{x}$, to the spectral radiance measured at the sensor, $\mathbf{y}$. This relationship can be written as

$$\mathbf{y} = F(\mathbf{x}) + \boldsymbol{\epsilon}, \tag{1}$$

where $\boldsymbol{\epsilon}$ accounts for measurement noise. The forward model predicts the measured radiance for a given surface and atmospheric state by simulating photon transport through the atmosphere using a radiative transfer model (RTM). The state vector represents the physically relevant parameters explicitly retrieved, while additional uncertainties arising from unresolved, unmodeled, or imperfectly characterized atmospheric processes are accounted for by the noise term.

Accordingly, an example state vector may be defined for each image pixel as

$$\mathbf{x} = [\rho_1, \rho_2, \ldots, \rho_n, \mathrm{x}_{\mathrm{AOT}}, \mathrm{x}_{\mathrm{H_2O}}]^T, \tag{2}$$

where $\rho_n$ denotes the surface reflectance in spectral channel $n$, while $\mathrm{x}_{\mathrm{AOT}}$ and $\mathrm{x}_{\mathrm{H_2O}}$ represent the aerosol optical thickness (AOT) at 550 nm and precipitable water vapor, respectively. Within this formalism, instrument-related parameters, such as corrections to the expected spectral calibration in each channel, can also be included as optimizable elements of the state vector.

In Thompson et al. (2024), such spectral calibration updates are parameterized by an interpolated cubic spline correction defined by four knot points, fixed at the extrema of the spectral range and at channels corresponding to wavelengths of 520 nm and 1790 nm. By optimizing these knot points, the model updates the spectral calibration to optimally fit atmospheric and surface absorption features with the radiative transfer model. This process yields spectral offsets at the specified spectral locations. The formulation is motivated by the expectation of a smooth, continuous perturbation of the initial calibration while retaining sufficient flexibility to capture systematic deviations in the spectral response.

Within the optimal estimation framework, the most probable state vector is obtained by minimizing the following cost function:

$$\chi^2(\mathbf{x}) = \frac{1}{2}(\mathbf{x} - \mathbf{x}_a)^T \mathbf{S}_a^{-1}(\mathbf{x} - \mathbf{x}_a) + \frac{1}{2}(\mathbf{y} - f(\mathbf{x}))^T \mathbf{S}_\epsilon^{-1}(\mathbf{y} - f(\mathbf{x})), \tag{3}$$

https://doi.org/10.5194/egusphere-2026-4701
Preprint. Discussion started: 14 August 2026


where $\mathbf{x}_a$ denotes the prior estimate of the state vector, $\mathbf{S}_a$ is the prior covariance matrix, and $\mathbf{S}_\epsilon$ is the noise covariance matrix.

The first term in the cost function constrains the solution toward physically plausible values based on prior knowledge, while the second term enforces consistency between the modeled and observed radiance, weighted by the expected measurement uncertainty. This formulation balances observational information and prior constraints, thereby stabilizing the inversion in the presence of noise and model nonlinearity.

### 3.2 Wavelength Calibration Input and Retrieval Methodology

All retrievals were based on instrument wavelength-calibration information provided to ISOFIT as an external text file specifying the nominal center wavelength and full width at half maximum (FWHM) for each spectral channel. These parameters define the spectral response functions used in the forward model and serve as the baseline spectral reference for all retrievals.

We followed the spline-based wavelength correction framework briefly introduced in Section 3.1. However, rather than adopting a fixed knot configuration, a systematic sensitivity analysis was conducted to investigate the effects of the number and placement of knot points on retrieval performance. Configurations employing between two and twelve knot points were evaluated, with knots distributed at various spectral positions across the instrument wavelength range. This range was chosen to establish clearly constrained cases at both lower and upper complexity limits while ensuring that an optimal configuration could be identified within these bounds. Configurations with too few knot points are expected to be overly restrictive, failing to fit atmospheric spectra accurately, whereas those with too many knots may be overly flexible, resulting in unstable or overfit solutions to specific scenes.

The dispersion profiles were compared with estimates derived from Zemax optical simulations (Bradley et al. (2020)), which provide a physically motivated reference for the instrument's expected wavelength behavior. Each configuration was applied consistently to the nine study scenes introduced in Section 2.2 to enable robust intercomparison across diverse observing conditions.

All retrievals were initialized using a flat wavelength dispersion profile, i.e., with channel wavelengths uniform in the spatial dimension and linear in the spectral dimension. This configuration served as a neutral initial condition from which wavelength corrections are iteratively refined during the inversion process. The spline representation enforces spectral smoothness while retaining sufficient flexibility to capture instrument-specific calibration deviations.

For configurations employing fewer than three knot points, the cubic spline was undefined. Instead, we used a first-order spline, resulting in piecewise linear interpolation between knot points. This ensured methodological consistency while permitting reduced-complexity representations of wavelength dispersion to be evaluated within a unified computational framework.

All retrieval experiments were performed using identical preprocessing procedures (Section 2.2.1), atmospheric priors, initial state vector values, and noise covariance specifications for a given image. While these inputs may differ between images to reflect scene-specific conditions, they were held fixed across all spline configurations within each image. Consequently, the forward-model configuration and atmospheric characterization remained consistent for each scene, ensuring that differences in the retrieval results arise solely from variations in the spline configuration.

https://doi.org/10.5194/egusphere-2026-4701
Preprint. Discussion started: 14 August 2026


## 4 Results

### 4.1 Model selection

This section examines the sensitivity of the retrieved wavelength-dispersion corrections to the chosen state-vector configuration, thereby assessing the robustness of the spline-based calibration framework. Specifically, we investigate whether the observed dispersion patterns primarily reflect intrinsic instrument behavior or arise from the selected spline knot configuration, including the number and spectral placement of knot points.

The atmospheric and instrument state vector elements for the nine scenes, obtained using a single retrieval configuration, are shown in Figure 2. All panels share the same horizontal axis, which indicates the cross-track position. The top row displays the retrieved atmospheric parameters: aerosol optical thickness (AOT), water vapor, and surface elevation offset, respectively. In this example, the instrument state vector is parameterized using six spline knot points located at predefined spectral channels, corresponding to the wavelengths indicated in the subplot titles and referenced relative to the initial wavelength calibration. The first and last knot points are positioned at the extrema of the spectral range. The atmospheric features show wide diversity, with aerosol optical depths ranging from clear skies (below 0.1) to hazy (near 0.4) and total precipitable water vapor ranging from dry (0.5 g $cm^{-1}$) to humid (3.0 g $cm^{-1}$). Nevertheless, the wavelength offsets are quite consistent across scenes, indicating a reliable retrieval of the sensor parameters, which are not expected to change significantly.

On a practical level, the investigation explored variations in both the number of spline knot points and their spectral placement. We define a *placement strategy* as the rule governing how knot locations are distributed across the spectrum, while a specific combination of placement strategy and total number of knots is hereafter referred to as a *sequence*. Four placement strategies were evaluated using between 2 and 12 knot points, resulting in a total of 44 sequences. All sequences share the common constraint that the first and last knots were fixed at the extrema of the spectral range. The first placement ("Even") strategy employed uniformly spaced knots across the spectrum. The remaining three strategies were initialized with four predefined knots, after which additional knots were iteratively inserted into the largest spectral gap between existing knots. Two of these strategies ("Strat 1" and "Strat 2") were constructed using informed heuristic choices, whereas the "On-Orbit" strategy was derived from the four knot locations reported by Thompson et al. (2024). The knot placement in the On-Orbit strategy was motivated by physical considerations, with knots positioned near the expected maxima of the second derivative of the dispersion profile.

The model selection is assessed using three performance metrics. The first performance metric is based on a comparison with an independent light-propagation simulation performed in Zemax OpticStudio, which serves as the reference solution for this analysis. Model performance is evaluated by summing the errors between the retrieval-derived dispersion profiles and the dispersion predicted by the Zemax simulation across all images. Although this simulation does not constitute a true ground truth, it provides a physically consistent, high-fidelity representation of the instrument response and is therefore used as a first-order check to ensure the results are reasonable.

https://doi.org/10.5194/egusphere-2026-4701
Preprint. Discussion started: 14 August 2026


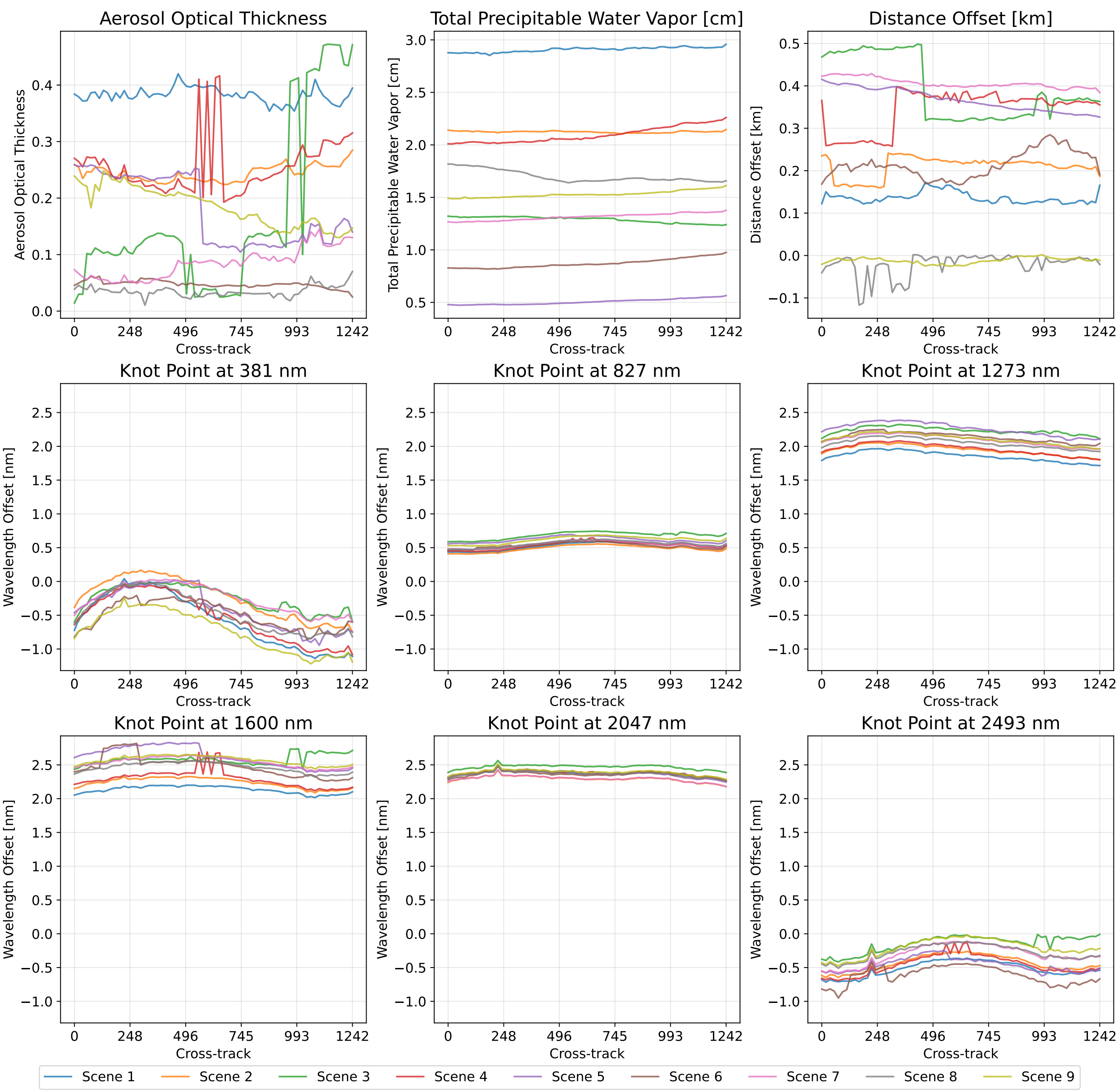


**Figure 2.** Retrieval results obtained using a six-knot cubic spline configuration with evenly distributed knot points. Color-coded curves represent retrievals from respective scenes. For all plots, the horizontal axis represents cross-track position, whereas the vertical axis represents atmospheric parameters (top row) and wavelength offsets (bottom two rows). The suggested wavelength offsets of -1 to 2.5 nm are relatively large and reflect the simplifying assumption of a spectrally flat initial dispersion curve in the wavelength calibration. (For interpretation of the references to color in this figure legend, the reader is referred to the web version of this article. )

https://doi.org/10.5194/egusphere-2026-4701
Preprint. Discussion started: 14 August 2026


To enable comparison, the retrieved wavelength offsets are converted into a wavelength dispersion profile. The offsets are applied to the nominal wavelength grid and subsequently interpolated using the same spline formulation as that implemented in the ISOFIT codebase, thereby constructing a continuous dispersion relation that maps wavelength to detector pixel position.

The resulting dispersion curves from each sequence were averaged across all nine images, yielding a single representative dispersion profile for each sequence. Figure 3 presents the results for all four sequences using 2, 4, 8, and 12 knots, respectively, with the Zemax simulation included for comparison. The discrete markers correspond to the retrieved wavelength offsets, whereas intermediate values are obtained via spline interpolation. Using only two knot points is insufficient to capture the expected complexity of the dispersion profile, whereas twelve knots introduce significant oscillations and reduce consistency across sequences.

Considering only the first performance metric, configurations using between four and eight knots exhibit the smallest differences relative to Zemax and comparable performance across all images. This suggests that these configurations achieve an optimal balance between model flexibility and stability.

The second performance metric assesses the consistency of the model's solution. As the number of spline points increases, each segment is governed by a smaller spectral interval having fewer potential absorption features to guide the fit. This could lead to inconsistent or underdetermined solutions, in which multiple spline configurations are equally consistent with the observed data. Visual inspection of Figure 3 indicates that sequences using four knots provide the most stable solution. In this case, all sequences produce nearly identical dispersion profiles, and no individual sequence clearly deviates from the others. As the number of spline points increases, the solutions become more erratic. The solution with 8 knot points is very sensitive to the precise placement of the knot points. The results for 12 knot points are even less consistent. This standard suggests that a simple cubic spline with about four knot points is appropriate for the information content of the measured VSWIR spectrum.

Our final performance metric assessed the ability of different wavelength solutions to match the spectra of a scene that was not used in the fitting process. Specifically, a leave-one-out cross-validation experiment was performed. Wavelength calibration results from eight images were averaged and then used to set the wavelength assignment for the ninth image. We then retrieved surface and atmospheric parameters for the ninth (held-out) scene and evaluated the cost function to quantify the spectral mismatch. This procedure was repeated for all images and model configurations, yielding a cross-validation metric for each spline-point configuration. The more accurate the wavelength calibration, the better its spectral fitting performance should be on a new scene.

Figure 4 shows the result of this process. The black bar shows the one-sigma dispersion of the nine different cross-validation trials. The range of chi-square scores varied widely across scenes, reflecting the specific noise and observing conditions present for each different observation. To isolate the impact of the wavelength calibration, we scale each scene's chi-squared curve to the [0,1] interval. Here, four knot points are clearly the best performing option. The narrow gray bar (i.e., the small spread of values) at 4 knot points suggests that the specific channel assignments of the knots do not strongly influence the outcome. With all three performance metrics indicating four knot points as the optimal configuration, this setting was adopted for the subsequent experiment. For backward compatibility and to enable comparisons in later stages, the On-Orbit sequence was employed.

https://doi.org/10.5194/egusphere-2026-4701
Preprint. Discussion started: 14 August 2026


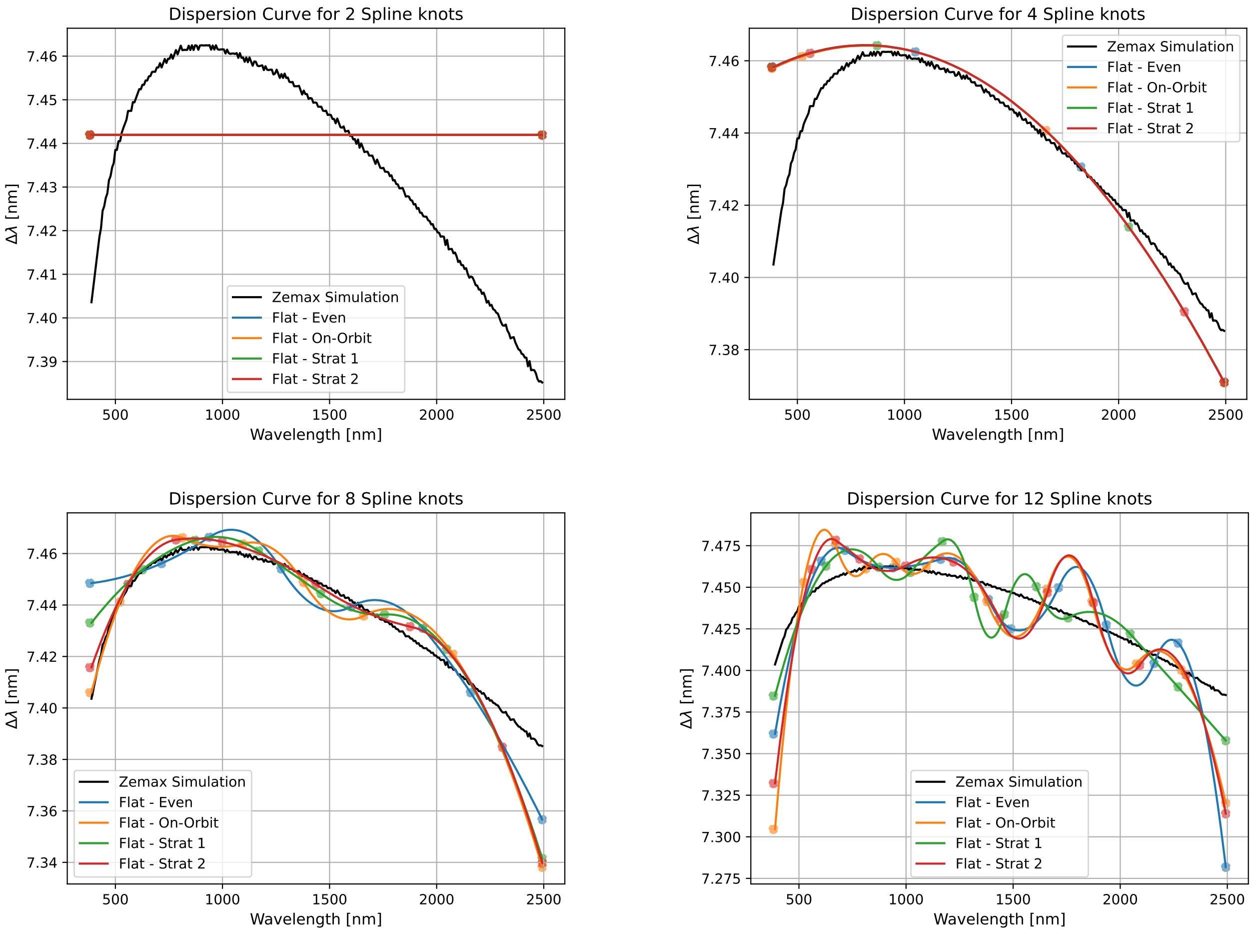


**Figure 3.** B-Spline interpolated wavelength dispersion curves based on four different knot sequences with two, four, eight and twelve spline knots. The coloured curves are shown for the 15th bin-averaged cross-track. A Zemax (light-propagation simulation software) reference dispersion curve for EMIT is plotted in black. (For interpretation of the references to colour in this figure legend, the reader is referred to the web version of this article.)

### 4.2 Cross-track dependent wavelength dispersion

Using the spline configuration identified through the model-selection analysis, this section examines the variability of the retrieved wavelength dispersion across the EMIT field of view. Taking the optimal number of four knot points obtained from the experiments above, we performed the calibration fitting process independently at each binned spatial position in the EMIT array. This is considerably more flexible than the common approach of a single wavelength for each channel, which assumes perfect spatial uniformity. It is even more expressive than a traditional “spectral smile“ plot, which describes cross-track

https://doi.org/10.5194/egusphere-2026-4701
Preprint. Discussion started: 14 August 2026


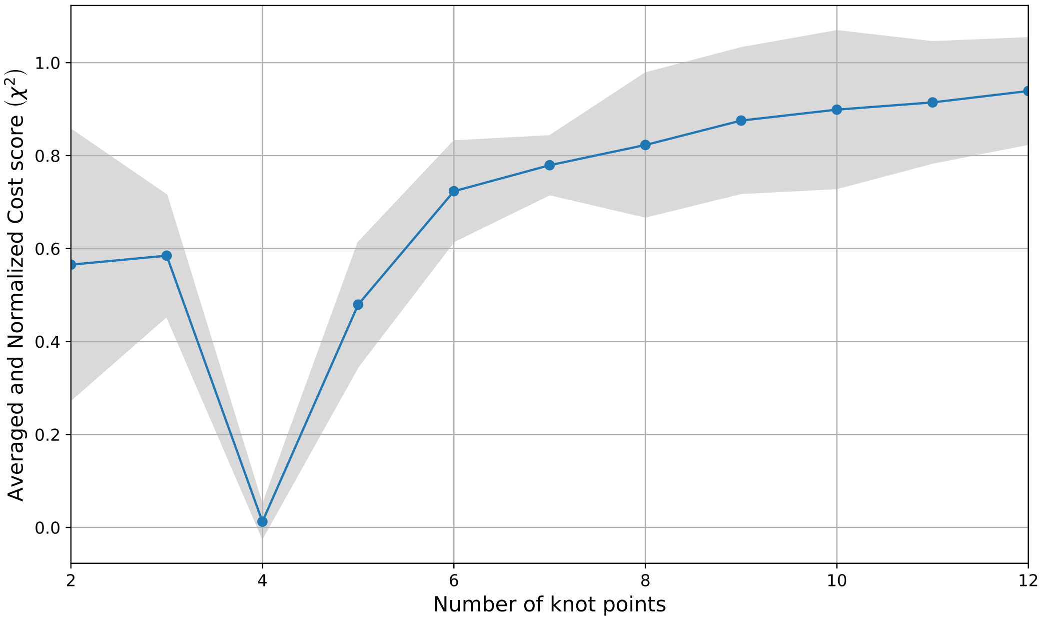


**Figure 4.** Averaged leave-one-out cross-validation (LOOCV) results are shown as normalized cost scores $\left(\chi^2\right)$ for the "On-Orbit" sequence using between 2 and 12 spline knot points across nine scene validation trials. Scores are scaled to the [0,1] interval to isolate wavelength-calibration effects. Gray bars indicate the one-sigma dispersion.

nonuniformity using a univariate shift. Here, in contrast, our procedure assigns a unique wavelength-center channel to each detector element.

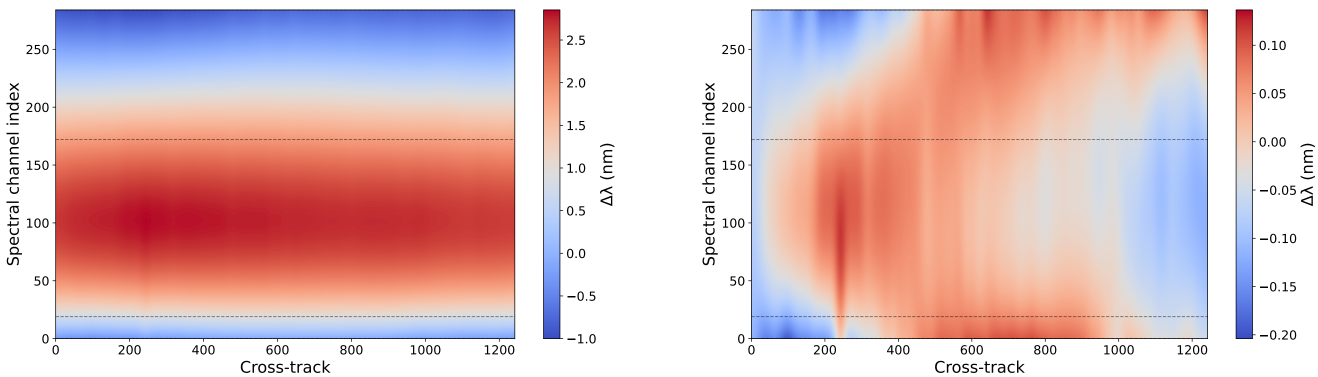


**Figure 5.** Left: Cubic spline interpolation with respect to the flat initial wavelength dispersion evaluated across the full sensor using spline parameters averaged over all nine scenes for the "On-Orbit" four knots configuration. Right: Same as the left panel, but with the cross-track mean subtracted from each column to highlight residual spatial variations.

https://doi.org/10.5194/egusphere-2026-4701
Preprint. Discussion started: 14 August 2026


The left panel of Figure 5 shows the retrieved wavelength corrections across the full sensor field of view. The two-dimensional plot represents the detector array, with the spectral dimension on the vertical axis and the spatial dimension on the horizontal axis. The left panel shows the deviation of the retrieved wavelength calibration from the initial assumption of a uniform dispersion. The color bands show the same basic polynomial curve that appears in Figure 3, but here repeats consistently at each cross-track position. Apart from one slight difference near position 240, the results are highly consistent for each independent fit. Position 240 is the location of a minor artifact in the flat field, believed to be a foreign object near the slit that resulted in a loss of signal over several detector columns at this location. The radiometric impact was mitigated with a change to the calibration flat field Thompson et al. (2024), but while the artifact is not generally visible in imagery, it reappears in certain highly sensitive analyses.

To better emphasize the spatial variability, the right panel of Figure 5 subtracts the cross-track average from each column. This is the error one would incur by using a single wavelength/channel assignment at every location, i.e., by assuming spatial uniformity. The error magnitudes are small — generally $1\%$ of a channel width or less across most of the array — but not laterally symmetric as previous smile plots Thompson et al. (2024) imply. Instead, we see a tilt from negative to positive at channel 250, which flips direction at the center of the array and then returns at small channel numbers. These variations indicate cross-track dependence in calibration, which could influence atmospheric correction or propagate into higher-level analysis products. This saddle-shaped distortion means that the right and left sides have very different calibrations, despite the smile plot suggesting they are similar. Any attempt to correct or account for spatial non-uniformity in this Dyson instrument would get far better results from a flexible, variable-dispersion model than a shift-based uniformity correction.

## 5 Discussion

Although this work presents a data-driven characterization of the EMIT instrument's spectral dispersion, it is important to recognize the limitations underlying the results. One key limitation arises from the forward model used in the retrieval framework, which relies on atmospheric absorption features to constrain the wavelength calibration. In the visible region of the spectrum, such features are relatively sparse and could reduce the sensitivity of the retrieval, leading to larger deviations from the Zemax simulation in this range.

A similar limitation occurs in spectral regions affected by strong atmospheric absorption, particularly around $\sim 1.4\ \mu m$ and $\sim 1.9 \mu m$ due to water vapor. In these bands, the reduced signal limits the retrieval's ability to reliably constrain the dispersion. As shown in Figure 3, the largest discrepancies between the retrieved dispersion curves and the Zemax simulation—especially for configurations using 8 and 12 spline knot points—are concentrated in these spectral regions.

Another limitation is the assumption that wavelength calibration was effectively constant over the duration of the study. While we have selected test scenes in close temporal proximity, it is possible that some wavelength drift could occur over this time. Occasionally, the instrument can experience thermal cycles due to periods of non-operation. While rare, these events could in theory cause small discrete jumps in wavelength calibration due to mechanical hysteresis. Consequently, the results presented in this study are expected to exhibit some temporal dependence and may differ if derived from data acquired at

https://doi.org/10.5194/egusphere-2026-4701
Preprint. Discussion started: 14 August 2026


a significantly earlier time. This interpretation is supported by intermediate retrieval results, where the estimated knot-point parameters for Scene 6 deviate noticeably from those of the other scenes.

The Zemax model-derived dispersion curve is based on an idealized optical model of the system, with all components in perfect alignment. Alignment with the Zemax model is thus a promising indicator that the atmospheric measurements produce valid dispersion profiles. However, the Zemax model should not be viewed as an unimpeachable source of ground truth - as with all calibration, the in-flight measurements are needed precisely because the model simplifies important aspects of the system, such as slight optomechanical misalignment. Here and elsewhere we find that calibration solutions constructed from real atmospheres, with the same radiative transfer model used for surface reflectance retrieval, are likely to produce better overall results than a calibration that relies solely on lab data.

The 0.1% discrepancies in wavelength calibration in Figure 5 may seem slight, but the impacts on surface retrievals are real. Thompson et al. (2021) find that even small sub-nanometer shifts can significantly impact certain retrieval algorithms in common use. Data-driven methods like partial least squares regression (PLSR) rely on subtle patterns between channels that are disrupted when those channels' interpretation changes. For even small non-uniformities, the bias induced by changing spectral calibration quickly exceeds instrument noise as a source of retrieval error. This suggests that future missions, such as EAGLE-VSWIR (Thompson et al., 2026), should maintain a cross-track dependent wavelength calibration with variable dispersion so that downstream algorithms can make full use of these data.

## 6 Conclusions

In this study, we applied a Bayesian Maximum A Posteriori (MAP) inversion framework using the ISOFIT radiative transfer retrieval system to jointly estimate atmospheric, surface, and instrument parameters from imaging spectroscopy data acquired by the Earth Surface Mineral Dust Source Investigation (EMIT) instrument. Within this physics-based framework, instrument spectral calibration is explicitly included as an optimizable component of the state vector, enabling wavelength-dispersion corrections to be directly inferred from EMIT-measured radiance while remaining constrained by radiative-transfer physics.

Building on this approach, we systematically evaluated how different spline-based representations of the instrument wavelength dispersion influence the retrieved solution. We varied both the number and placement of spline knot points across a diverse set of scenes and assessed performance using three complementary criteria: agreement with a high-fidelity Zemax OpticStudio simulation, solution stability across scenes and configurations, and predictive performance in a leave-one-out cross-validation framework.

Across all three metrics, a consistent optimum is identified at approximately four spline knot points. This configuration provides the most robust balance between flexibility and stability, closely reproducing the Zemax-derived dispersion profile while avoiding the oscillatory behavior and reduced consistency observed with increased numbers of spline knot points. Configurations with more knots increasingly suffer from greater sensitivity to knot placement and reduced cross-scene reproducibility, indicating that the additional degrees of freedom are not supported by the data's information content. In contrast, overly sparse configurations cannot capture the curvature of the dispersion profile.

https://doi.org/10.5194/egusphere-2026-4701
Preprint. Discussion started: 14 August 2026


The convergence of all evaluation criteria on the same optimal configuration suggests that the retrieved wavelength dispersion is well constrained and primarily reflects the underlying instrument response rather than artifacts of the spline parameterization. This provides a physically justified and empirically stable basis for subsequent analysis of cross-track wavelength variability.

Using this optimal model, we find that cross-track wavelength-dispersion variations are small, on the order of 1% of a spectral channel width. However, these deviations are not purely random: while subtle, they exhibit a coherent and structured spatial pattern. In particular, the spatial error field shows a weak but consistent saddle-shaped distortion across the detector array, rather than the laterally symmetric behavior previously assumed in simpler "smile"-style corrections. Although modest in absolute terms, this structured variability indicates that spatially uniform calibration assumptions are not strictly valid and that a spatially resolved wavelength model can provide a more accurate representation of the instrument response.

*Code and data availability.* The ISOFIT code for atmosphere and surface fitting, including dynamic wavelength calibration, is available at https://github.com/isofit/isofit-tutorials or https://doi.org/10.5281/zenodo.13968342 (archival link). In this study software Version 3.6.0 is used. Additionally, EMIT data are available at https://doi.org/10.5067/EMIT/EMITL1BRAD.001.

*Author contributions.* Mads J. Ahlebæk (MJA) and David R. Thompson (DRT) developed the research approach, methodology, performed the formal analysis, interpreted the results, prepared the figures, and wrote the original manuscript draft. MJA, DRT, Regina F. Eckert (RFE), Philip Brodrick (PB), Mads T. Frandsen (MTF), and Robert O. Green (ROG) contributed to the interpretation of the results, supervised the research, revised the manuscript, and approved the final version of the manuscript.

*Competing interests.*

The authors declare no competing interests.

*Acknowledgements.* A portion of this research was carried out at the Jet Propulsion Laboratory, California Institute of Technology, under a contract with the National Aeronautics and Space Administration (80NM0018D0004). The EMIT mission was sponsored by the NASA Earth Science Division. MJA acknowledges financial support from Otto Mønsteds Fond, Thomas B. Thriges Fond, William Demant Fonden, and Knud Højgaards Fond through travel grants that supported the JVSRP internship at JPL.

*Acknowledgement of AI Assistance.* Portions of this thesis have been developed with the assistance of AI-generated text such as ChatGPT and Grammarly. The AI was used to improve clarity, streamline the writing process, and provide suggestions for phrasing. All content has been carefully reviewed and edited to ensure accuracy, originality, and alignment with the papers objective.

https://doi.org/10.5194/egusphere-2026-4701
Preprint. Discussion started: 14 August 2026


## References

Bohn, N., Bair, E. H., Brodrick, P. G., Carmon, N., Green, R. O., Painter, T. H., and Thompson, D. R.: Do we still need reflectance? From radiance to snow properties in mountainous terrain: a case study with the EMIT imaging spectrometer, The Cryosphere, 19, 1279–1302, 2025.

Bradley, C. L., Thingvold, E., Moore, L. B., Haag, J. M., Raouf, N. A., Mouroulis, P., and Green, R. O.: Optical design of the Earth surface mineral dust source investigation (EMIT) imaging spectrometer, in: Imaging spectrometry XXIV: applications, sensors, and processing, vol. 11504, p. 1150402, SPIE, https://doi.org/10.1117/12.2568019, 2020.

Brodrick, P. G., Thompson, D. R., Fahlen, J. E., Eastwood, M. L., Sarture, C. M., Lundeen, S. R., Olson-Duvall, W., Carmon, N., and Green, R. O.: Generalized radiative transfer emulation for imaging spectroscopy reflectance retrievals, Remote Sensing of Environment, 261, 112 476, 2021.

Brodrick, P. G., Thompson, D. R., Bohn, N., Eckert, R., Montgomery, J., Wurster, K., and Vaughn, N.: ISOFIT Repository, https://doi.org/10.5281/zenodo.4614337, 2026.

D'Odorico, P., Alberti, E., and Schaepman, M. E.: In-flight spectral performance monitoring of the Airborne Prism Experiment, Applied optics, 49, 3082–3091, 2010.

Gao, B.-C., Montes, M. J., and Davis, C. O.: Refinement of wavelength calibrations of hyperspectral imaging data using a spectrum-matching technique, Remote Sensing of Environment, 90, 424–433, 2004.

Guanter, L., Richter, R., and Moreno, J.: Spectral calibration of hyperspectral imagery using atmospheric absorption features, Applied optics, 45, 2360–2370, 2006.

Haboudane, D., Miller, J. R., Tremblay, N., Zarco-Tejada, P. J., and Dextraze, L.: Integrated narrow-band vegetation indices for prediction of crop chlorophyll content for application to precision agriculture, Remote Sensing of Environment, 81, 416–426, https://doi.org/https://doi.org/10.1016/S0034-4257(02)00018-4, 2002.

Kuhlmann, G., Hueni, A., Damm, A., and Brunner, D.: An algorithm for in-flight spectral calibration of imaging spectrometers, Remote Sensing, 8, 1017, 2016.

Rodgers, C. D.: Inverse methods for atmospheric sounding: theory and practice, vol. 2, World scientific, 2000.

Scrivner, E., Mladenov, N., Biggs, T., Grant, A., Piazza, E., Garcia, S., Lee, C. M., Ade, C., Tufillaro, N., Grötsch, P., et al.: Hyperspectral characterization of wastewater in the Tijuana River Estuary using laboratory, field, and EMIT satellite spectroscopy, Science of the Total Environment, 981, 179 598, 2025.

Thompson, D. R., Boardman, J. W., Eastwood, M. L., Green, R. O., Haag, J. M., Mouroulis, P., and Van Gorp, B.: Imaging spectrometer stray spectral response: In-flight characterization, correction, and validation, Remote Sensing of Environment, 204, 850–860, 2018a.

Thompson, D. R., Natraj, V., Green, R. O., Helmlinger, M. C., Gao, B.-C., and Eastwood, M. L.: Optimal estimation for imaging spectrometer atmospheric correction, Remote sensing of environment, 216, 355–373, https://doi.org/10.1016/j.rse.2018.07.003, 2018b.

Thompson, D. R., Brodrick, P. G., Cawse-Nicholson, K., Dana Chadwick, K., Green, R. O., Poulter, B., Serbin, S., Shiklomanov, A. N., Townsend, P. A., and Turpie, K. R.: Spectral fidelity of Earth's terrestrial and aquatic ecosystems, Journal of Geophysical Research: Biogeosciences, 126, e2021JG006 273, 2021.

Thompson, D. R., Green, R. O., Bradley, C., Brodrick, P. G., Mahowald, N., Dor, E. B., Bennett, M., Bernas, M., Carmon, N., Chadwick, K. D., et al.: On-orbit calibration and performance of the EMIT imaging spectrometer, Remote Sensing of Environment, 303, 113 986, https://doi.org/10.1016/j.rse.2023.113986, 2024.

https://doi.org/10.5194/egusphere-2026-4701
Preprint. Discussion started: 14 August 2026


Thompson, D. R., Calvin, W. M., Ehlmann, B. L., Field, C. B., Pilewskie, P., Ustin, S. L., Brodrick, P. G., Chadwick, K. D., and Green, R. O.: The next era of remote spectral imaging of the Earth's surface, Nature Reviews Earth & Environment, pp. 1–2, 2026.

Thorpe, A. K., Green, R. O., Thompson, D. R., Brodrick, P. G., Chapman, J. W., Elder, C. D., Irakulis-Loitxate, I., Cusworth, D. H., Ayasse, A. K., Duren, R. M., et al.: Attribution of individual methane and carbon dioxide emission sources using EMIT observations from space, Science advances, 9, eadh2391, 2023.

van der Meer, F. D., van der Werff, H. M., van Ruitenbeek, F. J., Hecker, C. A., Bakker, W. H., Noomen, M. F., van der Meijde, M., Carranza, E. J. M., de Smeth, J. B., and Woldai, T.: Multi- and hyperspectral geologic remote sensing: A review, International Journal of Applied Earth Observation and Geoinformation, 14, 112–128, https://doi.org/https://doi.org/10.1016/j.jag.2011.08.002, 2012.

Yang, H., Kong, J., Hu, H., Du, Y., Gao, M., and Chen, F.: A review of remote sensing for water quality retrieval: Progress and challenges, Remote Sensing, 14, 1770, 2022.